Iranian Journal of Materials Science and Engineering, Vol. 22, Number 4, December 2025

RESEARCH PAPER

Investigation of the Static and Dynamic Mechanical Properties of the Base Metal and Weld Zone of Haynes 25 Alloy

Mahdi Behjati[1], Seyed Ali Asghar Akbari Mousavi[1], Yaser Vahidshad[2,*]

* *y.vahidshad@isrc.ac.ir*

[1] School of Metallurgy and Materials Engineering, College of Engineering, University of Tehran, Tehran, Iran
[2] Space transportation research institute, Iranian Space Research Center, Tehran, Iran

Received: September 2025 Revised: October 2025 Accepted: November 2025
DOI: 10.22068/ijmse.4355

Abstract: *This work presents a comprehensive investigation of the high-cycle fatigue behaviour of Haynes 25, a cobalt-based superalloy, and its pulsed continuous-wave (CW) laser-welded joints. The alloy, manufactured through vacuum induction melting and electroslag remelting followed by rolling and annealing, exhibited a yield strength of 650 MPa, an ultimate tensile strength of 1050 MPa, and an outstanding elongation of 57% at room temperature. The fatigue limit was determined by the test method to be 200 MPa for lifetimes exceeding* 10^8 *cycles, highlighting its excellent resistance to cyclic loading. For the weld zone, fabricated under optimised pulsed-CW laser parameters, the yield and ultimate tensile strengths were 660 MPa and 965 MPa, respectively, with a fatigue limit of 175 MPa. Advanced microstructural analyses using OM, SEM, EBSD, and XRD revealed an austenitic FCC matrix with carbide precipitates, predominantly* $(W, Cr)_7C_3$ *and* M_6C*, decorating both the matrix and grain boundaries. Fatigue crack initiation in the base metal was associated with carbide clusters near the surface, while in the weld zone, it was strongly linked to near-surface gas porosity defects. These findings not only establish fundamental fatigue benchmarks for Haynes 25 but also provide the first direct insights into the microstructural origins of fatigue damage in its laser-welded joints, thereby addressing a critical knowledge gap for its deployment in high-temperature and cyclic-loading environments.*

Keywords: *Haynes 25, Cobalt-based, Fatigue, Strength, Fractography.*

1. INTRODUCTION

Superalloys have been widely used for more than six decades in environments requiring high-temperature strength, stress tolerance, and corrosion resistance. Their applications span a broad range—from biomedical implants to advanced aerospace components. Based on chemical composition, these alloys are generally classified into three groups: nickel-based, iron–nickel-based, and cobalt-based systems [1–4].

Among cobalt-based superalloys, Haynes 25 is particularly noteworthy for its exceptional resistance to heat, corrosion, oxidation, nitridation, and wear. These properties, combined with good mechanical stability at elevated temperatures, have made it a common choice for gas turbines, jet engines, and chemical-processing equipment [5–7]. The alloy exhibits high phase stability, excellent oxidation resistance, and strong creep resistance, the latter enhanced by tungsten and nickel additions. Although cobalt-based alloys are less prevalent than nickel-based ones, they offer superior resistance to sulfidation and hot corrosion, prompting significant research into optimising the performance and processing of Haynes 25 [8–14].

Their microstructure strongly influences the performance of cobalt-based alloys. Haynes 25 and the related alloy Haynes 188 are recognized for their high ductility, oxidation resistance, and microstructural stability. Both contain approximately 0.1 wt% carbon, which promotes the formation of M_6C carbides that enhance strength without compromising ductility. Nickel additions lower the fcc/hcp transformation temperature and improve structural stability. While Haynes 25 is widely used in gas-turbine hot-section components, nuclear reactor parts, and surgical implants, Haynes 188 is specifically designed for high-temperature combustion environments, retaining excellent oxidation and creep resistance up to 1100°C [6, 15].

In cobalt-based alloys, several carbide types—including $M_{23}C_6$, M_6C, MC, and M_7C_3—may form depending on chromium, carbon, and other alloying elements. These carbides can improve strength but may also reduce ductility depending on their morphology and distribution.

Furthermore, topologically close-packed (TCP) phases such as σ, μ, R, and π can form during high-temperature exposure, generally reducing mechanical performance. Laves phases, observed in alloys such as L-605 (Haynes 25), are also detrimental due to their strong embrittling effect at elevated temperatures [10, 15–16].

Despite their advantageous high-temperature performance, cobalt-based superalloys remain susceptible to fatigue failure under cyclic loading. Fatigue behavior is highly sensitive to microstructure, carbide morphology, and phase stability. As advanced industries demand increasingly reliable high-temperature materials, improving fatigue resistance has become a critical objective. Previous research hav shown that carbide type and distribution, surface condition, and manufacturing processes—including heat treatments and optimized fabrication routes—strongly influence fatigue life [9, 18–28]. However, very few studies have explicitly focused on the mechanical and fatigue behavior of the weld zone in Haynes 25, despite the importance of welded components in high-temperature service environments [29]. This gap is particularly significant given that welding may alter microstructure, defect distribution, and mechanical response compared with the base metal.

To address this gap, the present study provides a comprehensive evaluation of the room-temperature mechanical properties and high-cycle fatigue behavior of Haynes 25 and its weld zone produced by pulsed continuous-wave laser welding. In addition, the high-temperature fatigue performance of both the base metal and weld zone is investigated to establish a complete understanding of their behavior under service-relevant conditions.

2. EXPERIMENTAL PROCEDURES

2.1. Raw Materials and Metal Preparation

The raw material was a square ingot of Haynes 25 alloy measuring 60×60 mm, produced by Vacuum Induction Melting (VIM) and subsequently refined by Electroslag Remelting (ESR). The ingot was then annealed, followed by hot-rolling in two perpendicular directions to achieve the target dimensions. A final recrystallisation anneal was performed to ensure uniform microstructure. To verify chemical homogeneity, samples were extracted from different positions along the ingot, and their chemical compositions are reported in Table 1.

2.2. Welding Procedure and Parameters

Laser welding was carried out using an ytterbium fiber laser system (model YLR), capable of operating in both continuous wave (CW) and pulsed modes, with a maximum power of 500 W. Welding was performed under optimized parameters [29], as summarized in Table 2.

2.3. Material Preparation and Testing

Cut specimens of the Haynes 25 superalloy were mounted and sequentially ground with sandpapers ranging from 80 to 1200 grit, followed by final polishing with diamond pastes of 0.3 and 0.1 µm. For microstructural examination, samples were etched in a solution of 15 mL HCl, 10 mL acetic acid, 5 mL HNO_3, and 2 drops of glycerin. After etching, the specimens were rinsed with pure methyl alcohol, dried with warm air, and observed under an optical microscope. Microstructural characterization was performed using a Leica optical microscope, with grain size measurements conducted on a Lietz microscope equipped with Image Analyzer software. For detailed microstructural and phase analysis, Energy-Dispersive X-ray Spectroscopy (EDS) was performed on a VEGA-TESCAN-LMU SEM, using high-magnification secondary electron imaging for surface mapping. Electron Backscatter Diffraction (EBSD) was carried out on a ZEISS GeminiSEM450 equipped with an Oxford Instruments EBSD detector to determine grain size, orientation, and boundary character, as well as to identify secondary phases.

Table 1. Chemical composition of Haynes 25 (L-605)

Co	Cr	W	Ni	Fe	Mn	Mo	Si	C	Al	Nb	V	Ti
50.35	19.02	13.60	11.74	3.09	1.31	0.61	0.14	0.09	0.02	0.01	0.01	<0.01

Table 2. Welded sample produced under the optimized parameters of the pulsed fiber laser welding process

Sample no.	Maximum power (W)	Pulse width (ms)	Welding speed (mm/s)	Frequency (Hz)	Mean power (W)	Pulse energy (J)	Heat input (J/mm)	Duty cycle %	Maximum effective power density (W/mm^2)	G×R (C/s)	G/R ($C.S/mm^2$)
13	450	20	5.6	30	270	9	48	60	1479	72992	2328

[DOI: 10.22068/ijmse.4355]

Samples for EBSD were prepared by grinding to 4000 mesh, followed by three-step polishing with 6, 3, and 1 μm diamond pastes and final vibratory polishing using a 0.25 μm colloidal silica suspension (OPS Struers). Phase identification was complemented by X-ray Diffraction (XRD) using a diffractometer operating over the 5°–130° angular range, with a step size of 2.6° and a 1 s per step delay. Diffraction patterns were analyzed using PANalytical X'Pert HighScore software.

Mechanical testing involved tensile and fatigue specimens sectioned by wire-cutting to 2 mm thickness, oriented perpendicular to the ingot thickness. Tensile tests of the base metal were conducted at room temperature on a Galdabini ball screw testing machine following ASTM E8 (Fig. 1a), providing mechanical property data for defining fatigue stress levels. Microhardness tests were performed in accordance with ASTM E384 using a 300 g load and a diamond indenter with a 136° apex angle. Fatigue tests on both base metal and weld specimens were carried out using Shimadzu Servopulser systems: one hydraulic machine with a 20-ton capacity at 10 Hz, and another with a 200 kN capacity capable of frequencies up to 30 Hz. Due to the specimen geometry and gripping configuration, all tests were conducted in a tension–tension mode. Specimens were designed with an arc-shaped cross-section, with the weld located at the specimen center (Fig. 1b). To minimize variables influencing fatigue life, such as stress concentration from surface roughness, all four specimen sides were ground to fully smooth the weld surface, finished to 600 grit, consistent with base metal preparation (Fig. 1c). The specimen ends were dog-bone shaped to ensure secure gripping, with the machine grips fully enclosing the head sections (Fig. 1d).

3. RESULT AND DISCUSSION

3.1. Morphology and Microstructure Analysis

Metallographic analysis of the base metal revealed an austenitic matrix containing dispersed carbide particles. The microstructure of the Haynes 25 superalloy (Figure 2) is characterized by a solid-solution austenitic matrix (gray regions) with a face-centered cubic (FCC) crystal structure. Consistent with literature and the Metallography Handbook, carbides of the types $M_{23}C_6$, M_6C, and M_7C_3 were identified within the matrix. High-magnification images (Figure 2a, b) show carbides distributed both along grain boundaries and within the austenite grains. Additionally, annealing twins formed during the heat treatment process were observed inside the grains (Figure 2c, d). The microstructure further indicates a non-uniform carbide distribution, often appearing as banded clusters throughout the alloy. SEM micrographs (Figure 2e) and EDS analysis (Figure 2f) show that the cobalt-based alloy has an austenitic (FCC) matrix, with $Cr_{23}C_6$ or $(W, Cr)_7C_3$ carbides present along the grain boundaries (point A).

As shown in Figure 3 and confirmed by Energy Dispersive X-ray Spectroscopy (EDS), most alloying elements exhibit an almost uniform distribution within both the matrix and grain boundaries (Figure 3a).

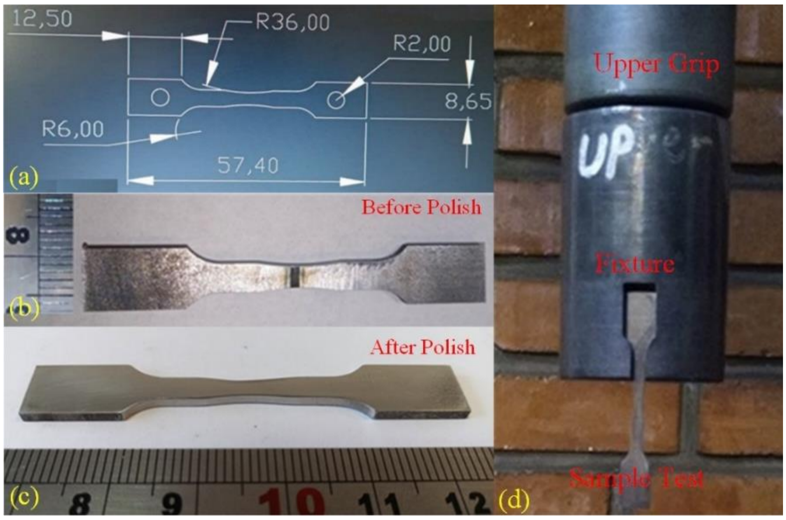

Fig. 1. a) Dimensions of the fatigue specimen, b) welded fatigue sample, c) polished fatigue sample, and d) fixture for fatigue testing

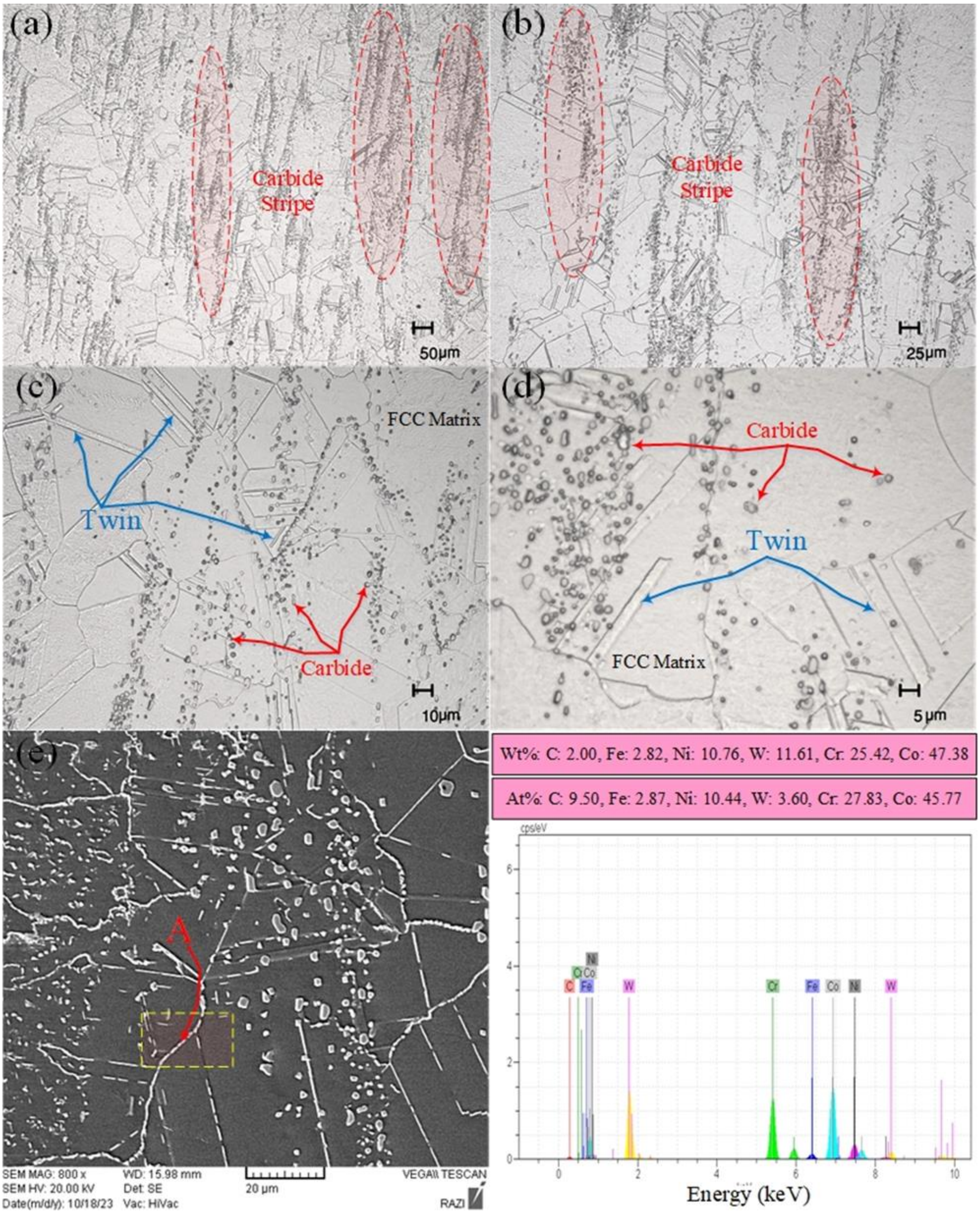

Wt%: C: 2.00, Fe: 2.82, Ni: 10.76, W: 11.61, Cr: 25.42, Co: 47.38

At%: C: 9.50, Fe: 2.87, Ni: 10.44, W: 3.60, Cr: 27.83, Co: 45.77

Fig. 2. Microstructural features of Haynes 25: a, b) carbide stripes along grain boundaries, c) FCC matrix with twins and carbides, d) higher magnification of twins and carbides, e) scanning electron microscope images of the base metal, f) energy-dispersive spectroscopy results of the A point

In contrast, tungsten shows a slightly non-uniform distribution, with localized tungsten-rich regions (Figure 3b), which can be attributed to the formation of tungsten-rich M_6C carbides in the base metal [27]. Meanwhile, cobalt (Figure 3c) and chromium (Figure 3d) display comparatively uniform distributions throughout the structure.

To gain deeper insight into the microstructure and

[DOI: 10.22068/ijmse.4355]

grain boundary characteristics, scanning electron microscopy (SEM) coupled with electron backscatter diffraction (EBSD) was employed to evaluate grain size distribution, crystallographic orientation, and grain boundary types. The results of the Electron Backscatter Diffraction (EBSD) analysis for the Haynes 25 alloy, including orientation maps, grain boundary maps, grain size distribution, Coincidence Site Lattice (CSL) boundary distribution, misorientation angle distribution, and texture analysis, are presented in Figures 5 and 6. Figure 4a illustrates the orientation map of the base metal. The Inverse Pole Figure (IPF) color map along the WD direction indicates that the grain orientations are random, consistent with the rolling and subsequent annealing heat treatment. Figure 4b shows that the matrix phase of Haynes 25 (highlighted in red) has a face-centered cubic (FCC) crystal structure.

At this scale, carbide precipitates such as (W, Cr)$_7$C$_3$ and Cr$_{23}$C$_6$ are not visible due to their fine size, though they are clearly observed in SEM images (Figure 3). The grain boundary distribution map (Figure 4c, d) reveals that high-angle grain boundaries (misorientation >15°) dominate the structure (blue), while low-angle boundaries (2–15°) account for less than 1% (red). Among the CSL boundaries (Figure 4e), Σ3, Σ5, Σ7, and Σ9 types were identified, with Σ3 boundaries comprising approximately 70%.

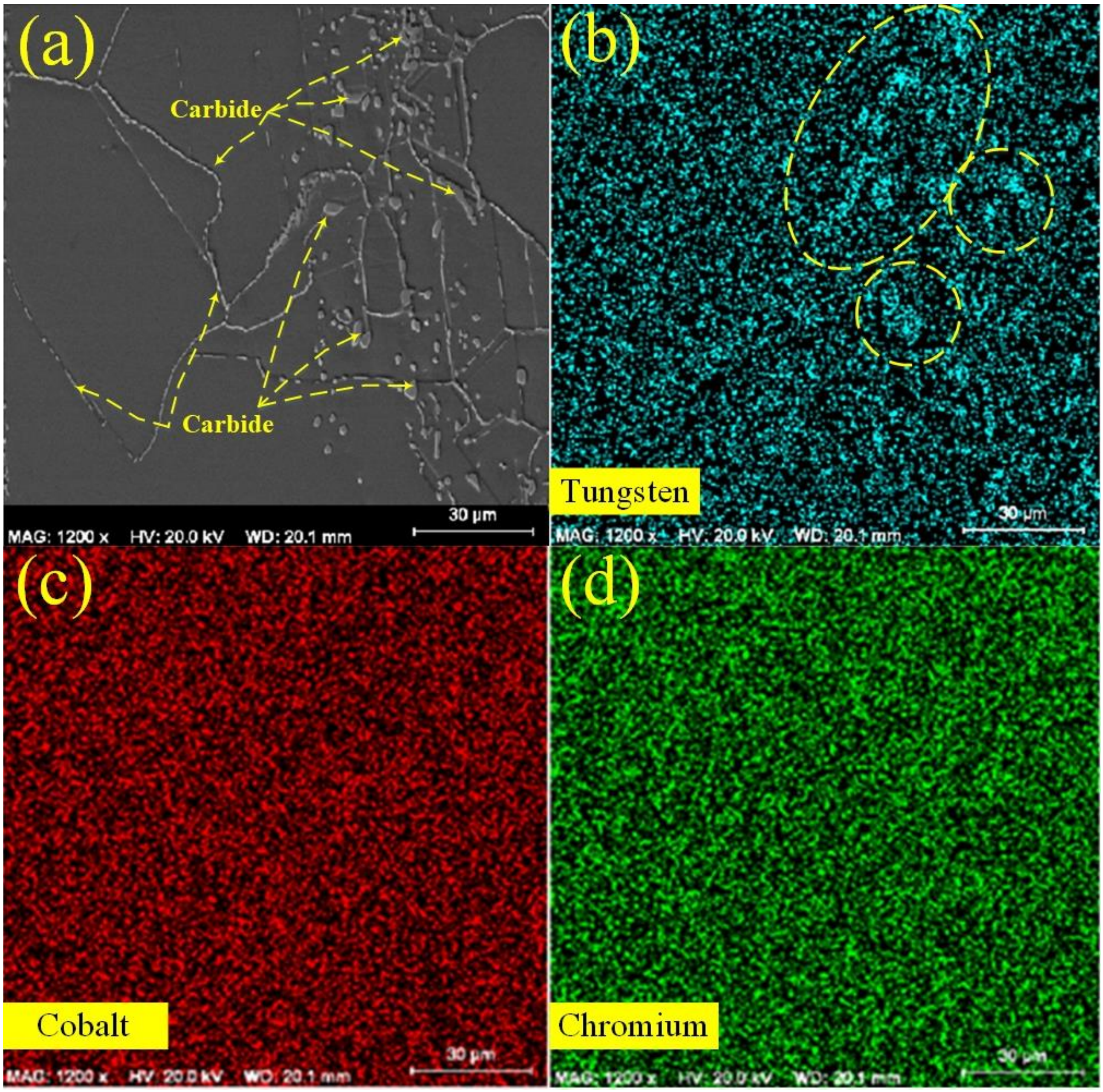

Fig. 3. SEM image and EDS maps of Haynes 25: a) carbides, b) tungsten, c) cobalt, d) chromium

[DOI: 10.22068/ijmse.4355]

The remaining high-angle boundaries are either random or Σ9 type (Figure 4f). Σ3 boundaries, characterized by a 60° misorientation about the <111> axis, correspond to annealing twins in FCC structures. Their high fraction suggests that extensive recrystallization and grain growth occurred during the annealing of the Haynes 25 ingot. The average austenitic grain size was measured at ~60 µm. Additionally, dendrites with parallel growth planes and a common growth direction were identified, while grain boundaries were clearly delineated through EBSD analysis. Figure 5 presents the inverse pole figure (Figure 5a) and pole figures (Figure 5b) for the Haynes 25 alloy. The inverse pole figure reveals that the dominant crystallographic texture is oriented along the <101> direction. Stereographic texture maps of the cobalt-based alloy are shown for the {001}, {101}, and {111} planes with respect to the X, Y, and Z axes. Based on the color scale representing distribution density, the preferred orientation is concentrated in the {101} planes. The pole figures further illustrate the orientation distribution across the three crystallographic planes of cobalt. In the {001} plane, the orientation density appears scattered, with a few localized red regions suggesting dispersed but significant orientations. In contrast, the {110} plane shows a higher density of orientation points, indicating that many grains preferentially align in this direction. The {111} plane also exhibits several regions of elevated density, though the distribution is more uniform than that of {110}.

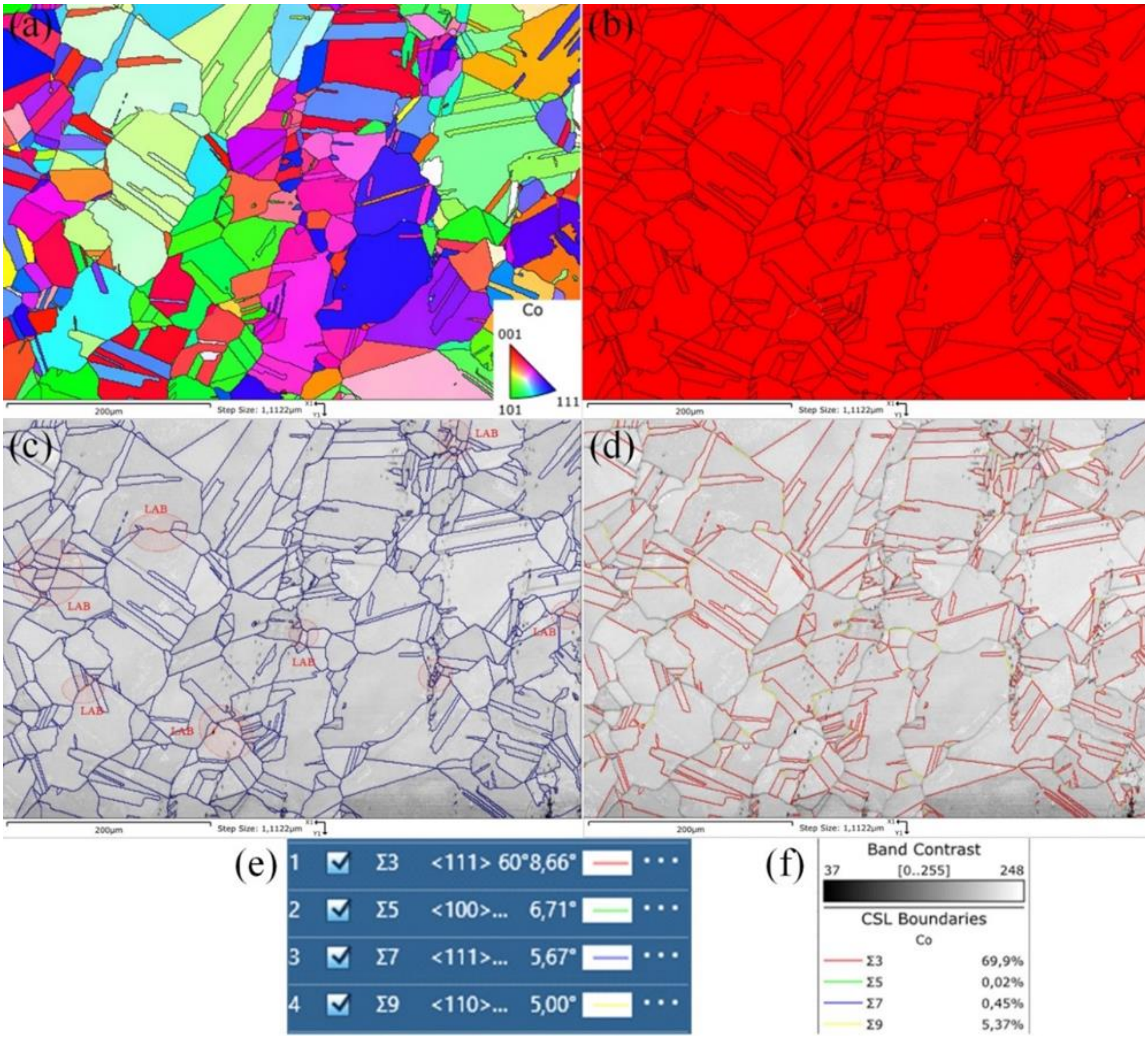

Fig. 4. EBSD maps of base metal: a) inverse pole figure (IPF) color, b) phase map, c) grain boundary distribution map d, e) coincidence site lattice and f) grain boundary distribution

[DOI: 10.22068/ijmse.4355]

[DOI: 10.22068/ijmse.4355]

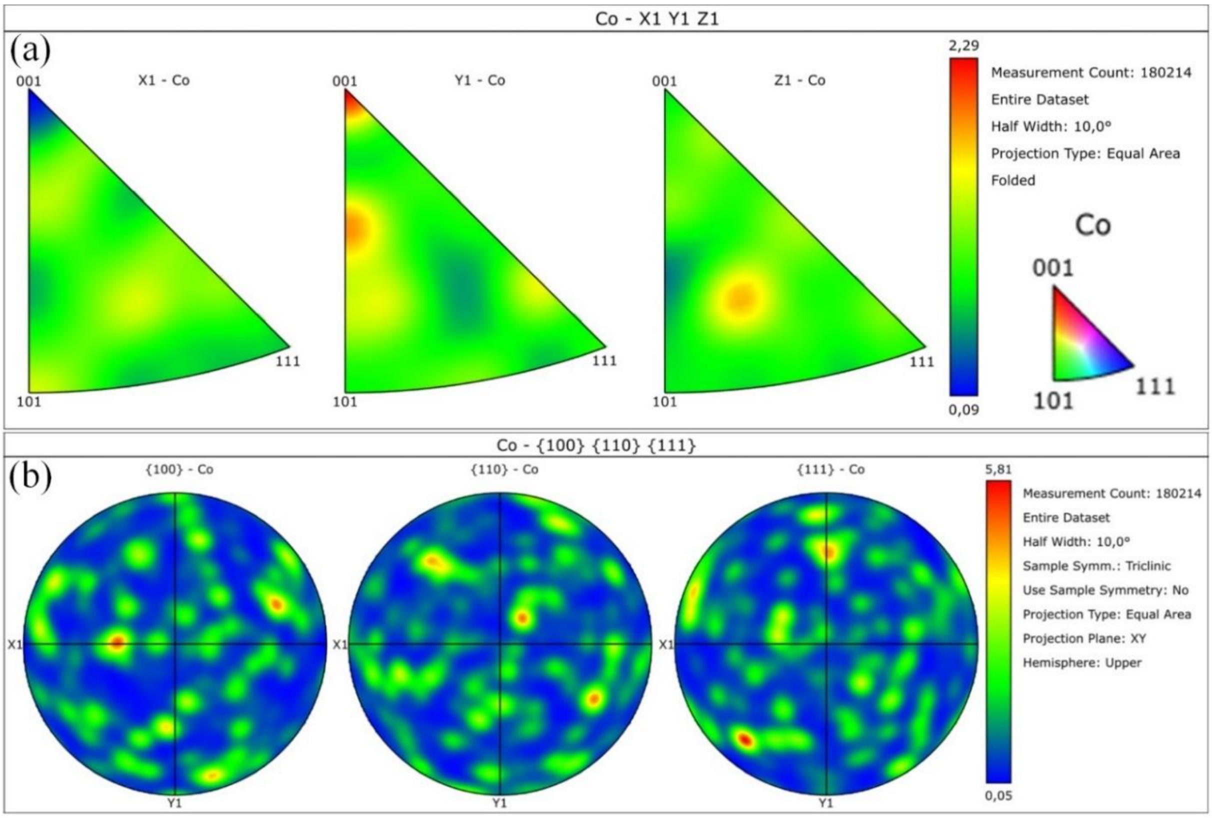

Fig. 5. EBSD maps of base metal: a) inverse pole figures and b) pole figures

3.2. Mechanical Properties Analysis

Tensile tests were conducted on both the Haynes 25 base alloy and the optimized welded sample at room temperature (Figure 6). The yield strengths of the base metal and the welded zone were 650 MPa and 660 MPa, respectively, while their ultimate tensile strengths (UTS) were 1050 MPa and 965 MPa, respectively. The elongation values were 57% for the base metal and 38.5% for the weld. The results indicate that a fracture during the tensile test occurred within the weld zone, and the measured strength was lower than that of the base metal. The coalescence of micropores in regions exhibiting localized strain discontinuities—such as those associated with second-phase particles, inclusions, or dislocation clusters—leads to pore growth and merging, eventually forming a continuous fracture surface as stress increases. The reduction in weld zone strength relative to the base metal is attributed to the heterogeneous distribution of high-density alloying elements such as tungsten, which tend to precipitate along grain boundaries and dendritic structures. Additionally, porosity and voids resulting from gas entrapment at the end of the laser-welding keyhole further contribute to the reduced strength of the weld zone.

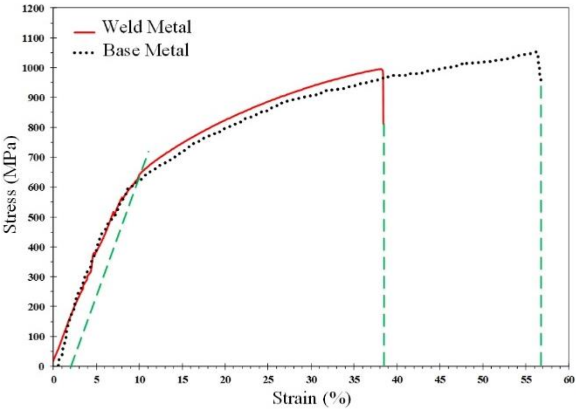

Fig. 6. Room temperature stress-strain graph of base metal and weld metal of the optimal welded sample

Stress was selected as the design criterion using the yield point with an appropriate safety factor, and the fatigue test stresses were set accordingly. The maximum stress levels the base metal and weld metal could sustain were 1100 MPa and 900 MPa, respectively, representing half-cycle loads. These values correspond to the highest stresses that the transverse-weld specimens could withstand and effectively reflect their tensile failure strengths at the weld. Fatigue testing was also performed on the base metal to evaluate its fatigue life. Five stress amplitudes were selected based on the tensile test results, ensuring all applied stresses were tensile. Among these, one stress level was below the yield strength, while the remaining four were above it. The applied stress amplitudes (ΔS), defined as the valley-to-peak of the sinusoidal stress curve, and the corresponding number of cycles to failure are summarized in Table 3. The maximum stress sustained for half a cycle (UTS) was approximately 1100 MPa. At a stress amplitude of 200 MPa, no fracture occurred even after prolonged cycling (Figure 7), indicating that this condition lies within the fatigue limit region, with a fatigue life exceeding 100 million cycles. This result aligns well with the findings of R.V. Marrey et al. [30], who reported a fatigue limit amplitude of 207 MPa for this alloy.

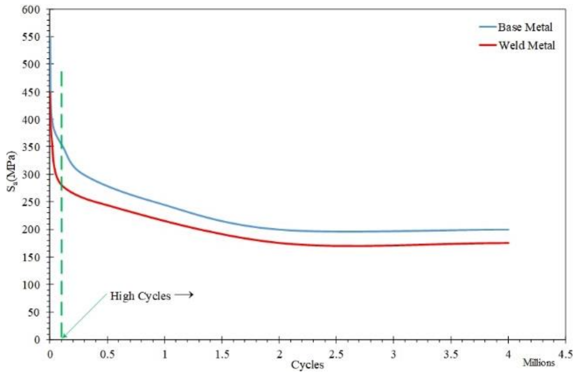

Fig. 7. Stress amplitude–fatigue life results of the base metal of Haynes 25 alloy (blue) and the weld zone of the alloy (red)

In long-cycle fatigue, 80–90% of life is spent on surface-crack nucleation, typically at stress concentrators such as residual stresses or weld defects (e.g., gas pores). All weld samples contained gas cavities, and those near the surface served as effective nucleation sites. Based on the table and graph, the fatigue strength ratio (weld/base metal) is higher in long cycles than in short cycles, indicating that at low stress levels, the weld behaves more like the base metal.

In the high-cycle (HCF) regime (exceeding 10^4–10^5 cycles), where applied stresses are low, fatigue is nucleation-controlled. In contrast, in the low-cycle (LCF) regime (generally below 10^4 cycles), where stresses are high, fatigue is crack-growth-controlled. Thus, HCF performance depends mainly on strength, while LCF performance depends on ductility. Therefore, improving resistance to crack nucleation at low stresses by minimising weld defects enhances long-cycle fatigue resistance. Accordingly, strength properties control performance in the high-cycle regime, while ductility governs the low-cycle regime [31]. Consequently, under low applied stresses, delaying crack initiation, achievable by minimizing weld defects, enhances fatigue resistance.

3.3. Fractography Analysis

Fractography of the fatigue fracture surfaces was examined using a stereomicroscope and a scanning electron microscope (SEM) for both the base metal and weld metal samples. At the microscopic level, the fatigue fracture surfaces exhibit crystalline features with striations, while the final sudden fracture (stage III) shows overload characteristics formed by microvoid coalescence, often containing carbide precipitates. Overload fracture features in metals resemble those observed in tensile fracture tests [32]. Multi-directional lighting was used to enhance visualization, as the fatigue crack growth region appears smoother and shinier than the sudden fracture zone due to contact between opposing crack surfaces [31].

As shown in Figure 8, the reduced (throated) regions correspond to the final overload fracture, whereas the thicker regions represent the fatigue crack growth zone, allowing unambiguous identification of the boundary between fatigue and final fracture.

Table 3. Fatigue test results of the base metal and the weld zone sample

Base metal	**ΔS MPa**	1100	800	700	600	500	400
	S_a MPa	550	400	350	300	250	200
	N_f	1	15800	112580	291000	914500	4000000>
	ΔS/S_y	2.34	1.70	1.49	1.28	1.06	0.85
Weld metal	**ΔS MPa**	900	740	570	500	350	
	S_a MPa	450	370	285	250	175	
	N_f	1	14617	85160	392900	4000000>	
	ΔS/S_y	1.91	1.57	1.21	1.06	0.74	

[DOI: 10.22068/ijmse.4355]

Tracing the crack path toward the concave center of the fracture surface made it possible to locate the crack initiation sites, indicated by arrows in Figure 8. Bright regions on the fracture surface correspond to carbide agglomerates, which act as barriers to dislocation motion and serve as preferred sites for fatigue crack initiation. Surface stress concentrations further promoted crack initiation at these carbides, assisted by persistent slip band (PSB) activity that produced crystallographic facets at the initiation points.

In Figures 8a and 8b, under low stress amplitudes, cracking initiated from a single site. With increasing stress, additional stress concentration sites became active, resulting in multiple crack origins, as observed in Figures 8c and 8d, where cracks initiated from both sides. The area of sudden (overload) fracture increased with higher stress amplitudes, reflecting the transition from fatigue crack growth to final catastrophic failure.

Figure 9 illustrates the fatigue fracture surfaces of the weld metal under varying stress amplitudes. Metallurgical defects, specifically gas pores, were observed in the fracture cross-sections, occupying approximately 7% of the total area. These pores reduce the effective load-bearing area, effectively increasing the nominal applied stress by a factor of 1.07, though design calculations typically consider the apparent cross-sectional area. Surface-near pores are more likely to act as fatigue crack initiation sites, and closely spaced porosities can amplify stress concentrations, promoting crack propagation [33-35]. At low stress levels (Figure 9a), cracks initiated at surface corners, with fatigue cracks propagating until final fracture. As stress increased (Figure 9b), two crack initiation sites appeared, while higher stress levels (Figure 9c) resulted in three to four initiation sites on the right side of the sample. In these cases, fatigue crack fronts propagated from both sides, with the final fracture zone forming near the center.

Haynes 25 alloys typically fail via microvoid coalescence. Microvoids form and grow in regions of localized strain discontinuity, such as around second-phase particles (carbides or intermetallics), inclusions, and dislocation clusters. As applied stress increases, these microvoids link to form a continuous fracture surface. The resulting cup-shaped depressions, or dimples, characterize ductile fracture. When multiple nucleation sites are activated, and adjacent voids coalesce early, small dimples of various shapes and sizes form, sometimes connected by shearing along slip bands. The shallow dimples observed in Figure 10a indicate ductile fracture with numerous microvoids of varying shapes and volumes. Cleavage or faceted fracture surfaces, also visible in Figure 10a, may arise from oxide inclusions or misaligned low-index crystallographic planes at grain or sub-grain boundaries.

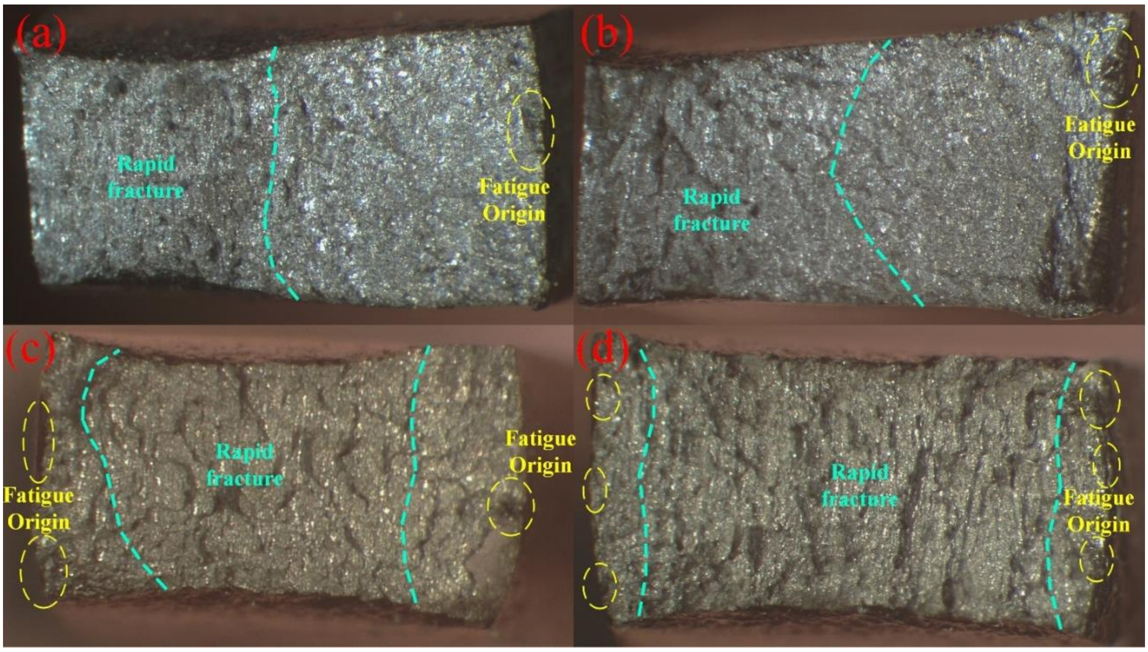

Fig. 8. Different loading orientations and crack propagation modes in the base metal at stress amplitudes of a) 250 MPa, b) 300 MPa, c) 350 MPa, and d) 400 MPa

[DOI: 10.22068/ijmse.4355]

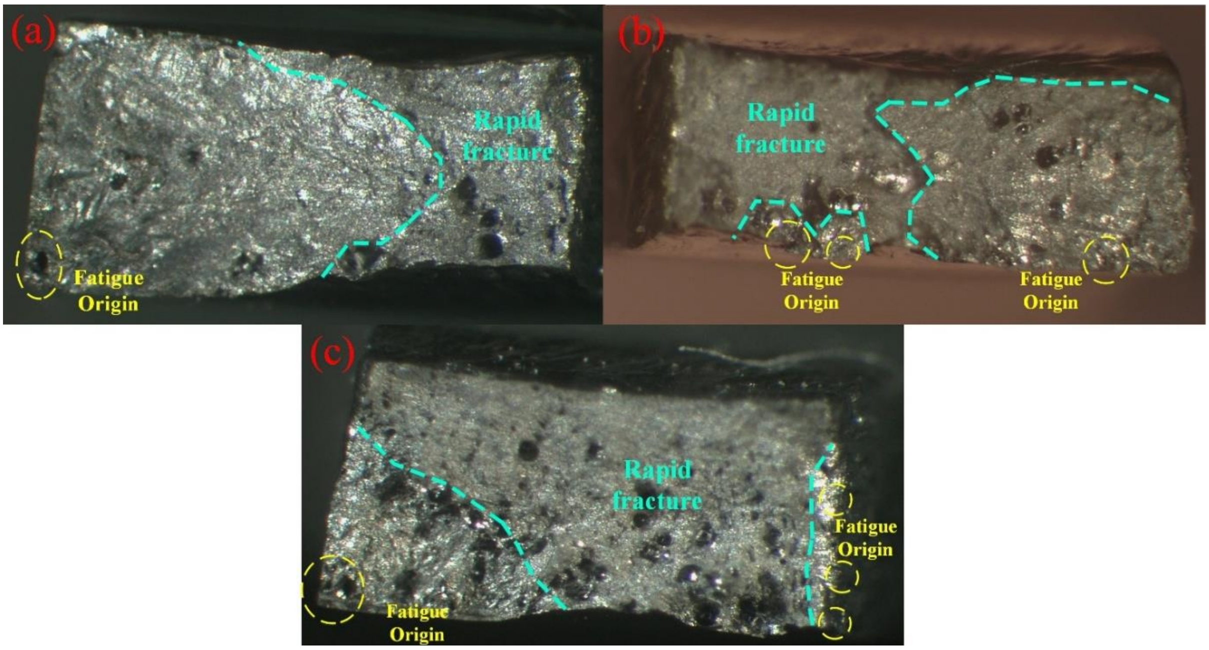

Fig. 9. Different loading orientations and crack propagation modes in the weld metal at stress amplitudes of a) 250 MPa, b) 285 MPa, and c) 370 MPa

Cleavage planes are generally observed as bright or white regions on the fracture surface. Microscopic examination of fatigue fracture surfaces revealed typical beach marks or river patterns (Figure 10b), with clearly visible microcracks during the fatigue stage. The final sudden fracture stage (Figure 10c) resembles tensile fracture surfaces (Figure 10a). Volumetric defects, such as microvoids, trapped-gas pores, and structural flaws, were observed on the final fracture surfaces of both tensile and fatigue tests. A quantitative fracture analysis using image-processing segmentation of the SEM micrographs shows (Figure 10c) that, in the final fracture region of the fatigue specimen tested under 300 MPa cyclic stress, less than 30% of the surface corresponds to brittle cleavage or faceted features, while more than 70% consists of ductile dimple morphology.

Microscopic examination of the fatigue fracture surfaces reveals that increasing stress amplitude leads to a more pronounced presence of micro-cracks (Figure 11a, b, c and d). SEM images show that as the stress amplitude rises from 250 MPa to 400 MPa, the number of secondary cracks increases. Additionally, the spacing of striations, or beach marks, widens with increasing stress amplitude. The schematic in Figure 11e illustrates this effect:

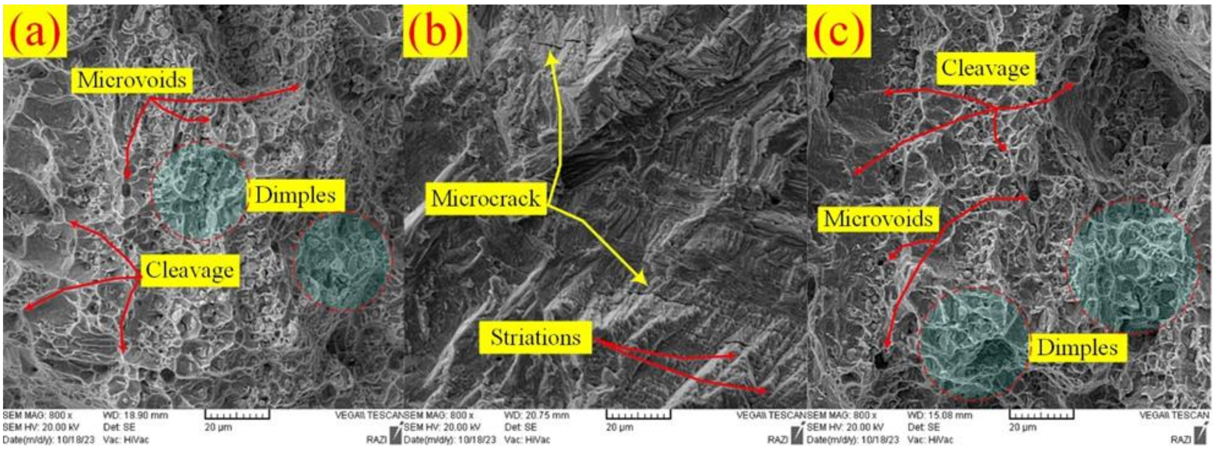

Fig. 10. SEM images of base metal fracture surfaces: a) tensile test specimen, b) fatigue specimen, c) final fracture of fatigue specimen under 300 MPa cyclic stresses

[DOI: 10.22068/ijmse.4355]

Higher stress amplitudes enhance displacement along the 45° shear slip planes and increase plastic deformation at the crack tip, thereby increasing the fatigue striation spacing. Figure 11d, f presents Energy Dispersive Spectroscopy (EDS) analysis of precipitates on the fracture surface of the base metal. The presence of alloying elements, chromium (29 at%), nickel (6 at%), tungsten (14 at%), and carbon (14 at%), confirms the formation of carbide compounds, particularly (Cr, Ni, W)$_7$C$_3$.

Metallurgical defects in the weld significantly reduce fatigue life. Figure 12 shows SEM images of the weld-zone fracture surfaces, which exhibit gas porosity defects. Analysis indicates that fatigue cracks in the welded samples (Figure 12a) originated at these surface or near-surface gas pores (Figure 12b). In contrast, fatigue crack initiation in the base metal occurred at carbide clusters near the surface, particularly at corners. Higher-magnification images (Figure 12c) show striation lines inclined toward a gas pore at the specimen corner, confirming that fatigue failure initiated in that region. Examination of the internal surfaces of the pores reveals striations extending into the pore (Figure 12d). Due to the concave geometry, the inner pore surface remains untouched by the opposing fracture surface, resulting in concentric-like lines indicative of fatigue crack propagation.

4. CONCLUSIONS

This study thoroughly evaluated the static and fatigue properties of Haynes 25 cobalt-based superalloy and its weld zone produced via pulsed continuous-wave laser welding. The base metal exhibited a yield strength of 650 MPa, ultimate tensile strength of 1050 MPa, and elongation of 57%, with a fatigue limit of 200 MPa for lives exceeding 10^8 cycles. The weld zone showed a slightly higher yield strength (660 MPa) but lower ultimate strength (965 MPa) and ductility (38.5%), with a fatigue limit of 175 MPa.

Microstructural analysis revealed an austenitic FCC matrix with carbide precipitates, mainly (W, Cr)$_7$C$_3$ and M$_6$C. In the base metal, carbide clusters served as primary fatigue crack initiation sites, whereas in the weld zone, cracks predominantly originated at near-surface gas pores, highlighting the adverse effect of welding-induced defects. Striation spacing increased with stress amplitude, reflecting greater plastic deformation at crack tips.

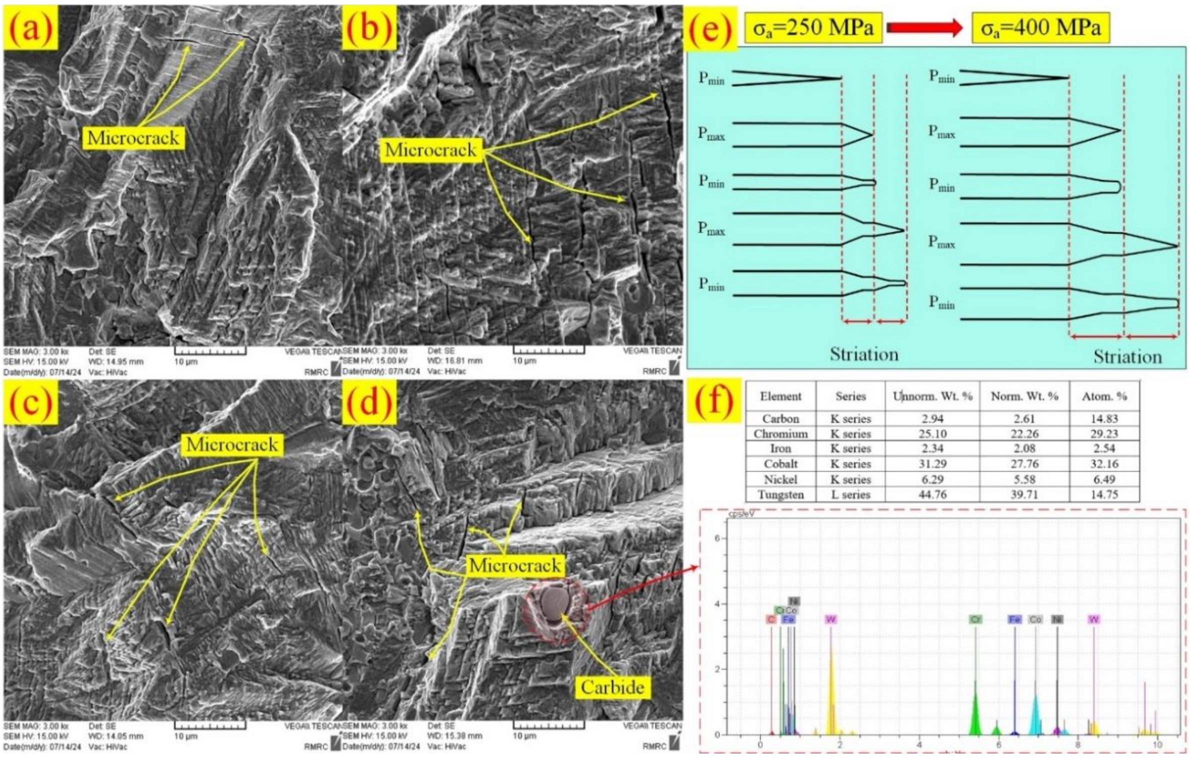

Element	Series	Unnorm. Wt. %	Norm. Wt. %	Atom. %
Carbon	K series	2.94	2.61	14.83
Chromium	K series	25.10	22.26	29.23
Iron	K series	2.34	2.08	2.54
Cobalt	K series	31.29	27.76	32.16
Nickel	K series	6.29	5.58	6.49
Tungsten	L series	44.76	39.71	14.75

Fig. 11. Fatigue fracture surface of base metal fatigue specimens at stress amplitudes of: a) 250 MPa, b) 300 MPa, c) 350 MPa, and d) 400 MPa, e) effect of stress amplitude on the spacing of striations, f) energy-dispersive spectroscopy result of the carbide

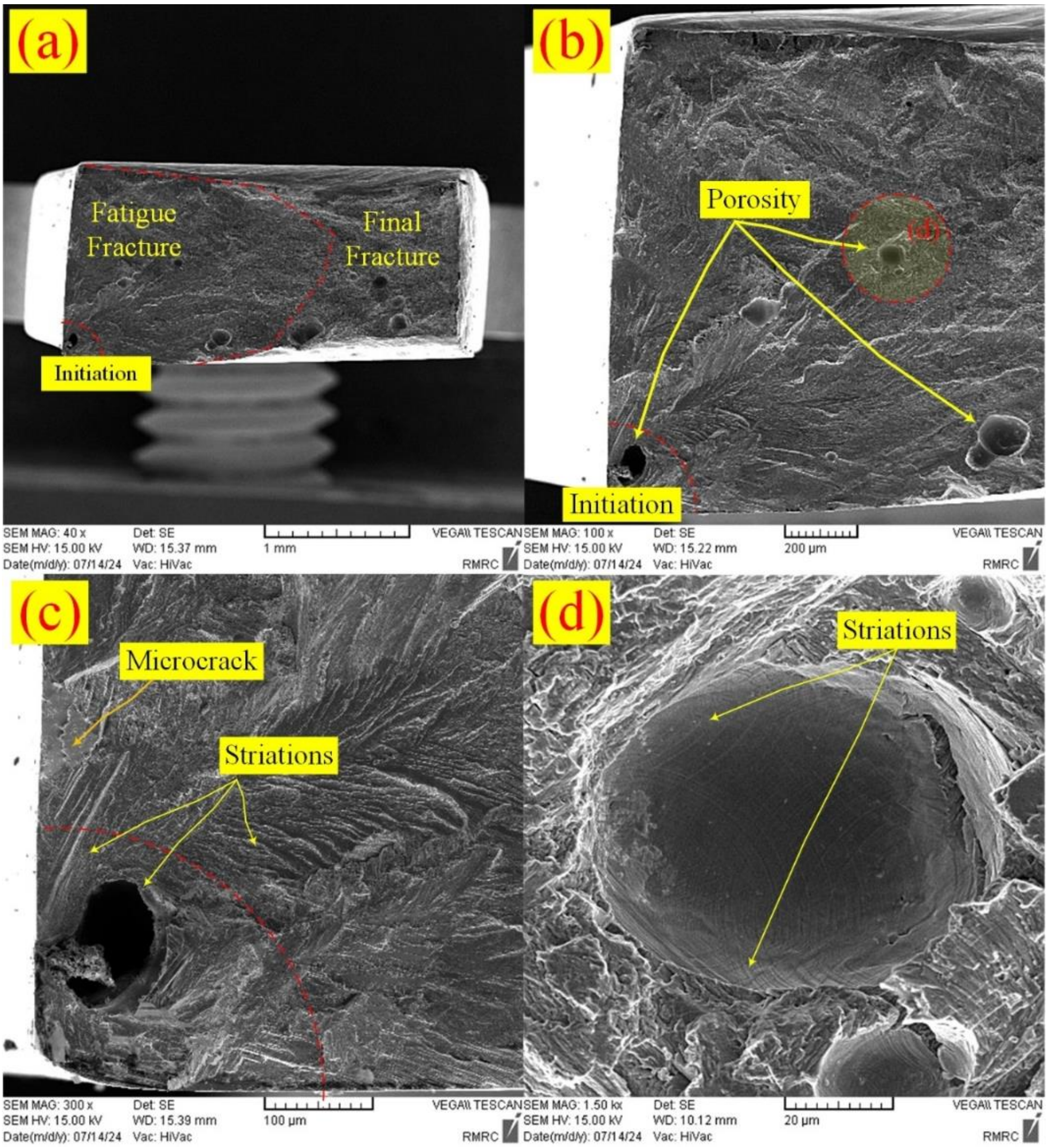

Fig. 12. Fatigue fracture surface of weld metal fatigue specimens at stress amplitude of 250 MPa

Overall, while laser welding produces joints with mechanical properties close to those of the base alloy, weld porosity significantly reduces fatigue performance. Minimizing gas pore formation is therefore essential for improving the high-cycle fatigue resistance of Haynes 25 components in demanding applications.

ACKNOWLEDGEMENTS

We are deeply grateful to Mr Fereidoun Tosynejad, an expert in the metallography laboratory of the Space Transportation Research Institute, who contributed greatly to this research.

REFERENCES

[1] Reed, R. C., "The super alloys: fundamentals and applications", Cambridge University Press, 2006, pp. 1-28.

[2] Donachie, M. J., Donachie, S. J., "Superalloys for high temperatures- a primer in superalloys: A technical guide", ASM International, 2002, pp. 1-9.

[3] Minouei, H., Fathi, M., Meratian, M., Ghazvinizadeh, H., "Heat treatment of cobalt-base alloy surgical implants with hydroxyapatite-bioglass for surface bioactivation", Iran. J. Mater. Sci. Eng.,

2012, 9, 33-39. doi: ijmse.iust.ac.ir/article-1-174-en.html.

[4] Razavi, N. Avanzini, A., Cornacchia, G., Giorleo, L., Berto, F., "Effect of heat treatment on fatigue behavior of as-built notched Co-Cr-Mo parts produced by Selective Laser Melting", Int. J. Fatigue, 2021, 142, 105926. doi: 10.1016/j.ijfatigue.2020.105926.

[5] Zhu, Z., Chen, L., "Effect of annealing on microstructure and mechanical properties of biomedical hot-rolled Co-Cr-W-Ni alloy", Mater. Res. Express, 2019, 6, 1-11. doi: 10.1088/2053-1591/ab546c.

[6] Davis, J. R., ASM speciality handbook, "Nickel, Cobalt, and Their Alloys", ASM handbook, Materials Park, OH 44073, 2000, pp. 343-386.

[7] Hira, U., Maqsood, N., "Super alloy: Fundamentals and Applications-Cobalt based Superalloy", Materials Research Foundations, 2025, 178, 68-80. doi: 10.21741/9781644903698-4.

[8] Samii Zafarghandi, M., Abbasi, S.M., Momeni, A., "Effects of Nb on hot tensile deformation behavior of cast Haynes 25 Co-Cr-W-Ni alloy", J. Alloy. Compd., 2019, 774, 18-29. doi: 10.1016/j.jallcom.2018.09.301.

[9] Donachie, M. J., Donachie, S. J., "Superalloys: A Technical Guide", ASM International, 2002. pp. 25-38.

[10] Nathal, M. V., "Effects of microstructure on the creep properties of cobalt-based superalloys", Metall. Mater. Trans. A, 1990, 21, 2319-2328. doi: 10.1016/j.msea.2016.09.060.

[11] Sims, C. T., "High-temperature materials for power engineering", Elsevier, 2001, pp. 123-130.

[12] Adiban, S.V., Ramu, M., "Study on the effect of weld defects on fatigue life of structures", Mater. Today: Proceedings, 2018, 5, 17114-17124. doi: 10.1016/j.matpr.2018.04.119.

[13] Quazi, M. M., Ishak, M., Fazal, M. A., Arslan, A., Rubaiee, S., Aiman, M. H., Qaban, A., Yusof, F., Sultan, T., Ali, M.M., Manladan, S. M., "A comprehensive assessment of laser welding of biomedical devices and implant materials: recent research, development and applications", Crit. Rev. Solid State Mater. Sci., 2021, 46, 109-151. doi: 10.1080/10408436.2019.1708701.

[14] Ajami Ghaleh Rashidi, P., Arabi, H., Abbasi, S.M., "Effect of cold-rolling on mechanical properties of haynes 25 cobalt-based superalloy", Metall. Mater. Eng., 2017, 23, 31-45, 2017. doi: 10.30544/248.

[15] Kumar, S., "Technology of Metal Forming Processes", PHI Learning Pvt. Ltd., 2008, pp. 1-19.

[16] Shahriary, M. S., Gorji, Y. M., Kolagar, A. M., "Gas metal arc welding in refurbishment of cobalt base superalloys", IOP Conf. Ser.: Mater. Sci. Eng., 2017, 164, 012016. doi: 10.1088/1757-899X/164/1/012016.

[17] Lee, B. S., Matsumoto, H., Chiba, A., "Fractures in tensile deformation of biomedical Co–Cr–Mo–N alloys", Mater. Lett., 2011, 65, 843-846, 2011. doi: 10.1016/j.matlet.2010.12.007.

[18] Jiang, L., Wang, H., Liaw, P.K., Brooks, C.R., Chen, L., Klarstrom, D.L., "Temperature evolution and life prediction in fatigue of superalloys", Metall. Mater. Trans. A, 2004, 35A, 839-848. doi: 10.1007/s11661-004-0010-2.

[19] Pollock, T. M., Tin, S., "Nickel-based superalloys for advanced turbine engines: Chemistry, microstructure and properties", J. Propuls. Power, 2006, 22, 361-374. doi: 10.2514/1.18239.

[20] Karthick, M.P.G., Annamalai A, R., Mohanty, C.P., Chauhan, A.S., "Low-cycle fatigue behavior of as-cast and heat-treated Haynes 25 superalloy under varying strain amplitudes", Results Eng., 2025, 28, 107089. doi: 10.1016/j.rineng.2025.107089.

[21] Chen, L.J., Liaw, P.K., He, Y.H., Benson, M.L., Blust, J.W., Browning, P.F., Seeley, R.R., Klarstrom, D.L., "Tensile hold low-cycle fatigue behavior of cobalt-based HAYNES-188 superalloy", Scr. Mater., 2001, 44, 859-865. doi: 10.1016/S1359-6462(00)00702-8.

[22] Sweeney, C.A., O'Brien, B., Dunne, F.P.E., McHugh, P.E., Leen, S.B., "Strain-gradient modelling of grain size effects on fatigue of CoCr alloy", Acta Mater., 2014, 78, 341-353. doi: org/10.1016/j.actamat.2014.06.044.

[23] Alfred J. Nachtigall, Stanley J. Klima, John C. Freche, and Charles A. Hoffman, "The effect of vacuum on the fatigue and stress-

[DOI: 10.22068/ijmse.4355]

rupture properties of S-816 and Inconel 550 at 1500°F", NASA technical note, 1965, NASA TN D-2898.

[24] Lu, Y., "High-temperature low-cycle-fatigue and crack-growth behaviors of three superalloys: Hastelloy X, Haynes 230, and Haynes 188", The University of Tennessee, 2005.

[25] Kataria, R., Singh, R.P., Sharma, P., Phanden, R.K., "Welding of super alloys: A review", Mater. Todays, 2021, 38, 265-268. doi: 10.1016/j.matpr.2020.07.198.

[26] Gedwill, M. A., "Thermal fatigue behavior of cobalt-based superalloys", NASA Technical Paper 1854, 1981.

[27] Buckson, R.A., Ojo, O.A., "Cyclic deformation characteristics and fatigue crack growth behaviour of a newly developed aerospace superalloy Haynes 282", Mater. Charact., 2012, 555, 63-70. doi: 10.1016/j.msea.2012.06.034.

[28] Lee, S.Y., Lu, Y.L., Liaw,P.K., Chen, L.J., Thompson, S.A., Blust, J.W., Browning, P.F., Bhattacharya, A.K., Aurrecoechea, J.M., Klarstrom, D.L., "Hold-time effects on elevated-temperature low-cycle-fatigue and crack-propagation behaviors of HAYNES 188 superalloy", J. Mater. Sci., 2009, 44, 2945-2956. doi: 10.1007/s10853-009-3391-1.

[29] Abbasi R., Akbari Mousavi S.A., Vahidshad Y., "Optimization weldability of Haynes 25 cobalt base superalloy with pulsed fiber laser", Journal of Welding Science and Technology, 2024, 10, 83-97. doi: 2010.47176/JWSTI.2024.19.

[30] Marrey, R.V., Burgermeister, R., Grishaber, R.B., Ritchie, R.O., "Fatigue and life prediction for cobalt-chromium stents: A fracture mechanics analysis", Biomater., 2006, 27, 1988-2000. doi: 10.1016/j.biomaterials.2005.10.012.

[31] Stephens, R.I., Fatemi, A., Stephens, R.R., Fuchs, H.O., Metal fatigue in engineering, John Wiley & Sons, INC., 2001, pp. 33-57.

[32] Khatibi, G., Lederer, M., Betzwar Kotas, A., Frotscher, M., Krause, A., Poehlmann, S., "High-cycle fatigue behavior of thin-walled CoCr tubes", Int. J. Fatigue, 2015, 80, 103-112. doi: 10.1016/j.ijfatigue.2015.05.013.

[33] diban, S.V., Ramu, M., "Study on the effect of weld defects on fatigue life of structures", Mater. Today, 2018, 5, 17114-17124. doi: 10.1016/j.matpr.2018.04.119.

[34] Paul, M., Ghiaasiaan, R., Grad, P., Caron, J., Wang, P., Shao, S., Shamsaei, N., "Tensile and fatigue behaviors of newly developed HAYNES® 233 alloy: Additively manufactured vs. wrought", Mater. Des., 2024, 244, 113165, doi: 10.1016/j.matdes.2024.113165.

[35] Karthick, M.P.G., Annamalai A, R., Mohanty, C.P., Chauhan, A.S., "Low-cycle fatigue behavior of as-cast and heat-treated Haynes 25 superalloy under varying strain amplitudes", Results Eng., 2025, 28, 107089, doi: 10.1016/j.rineng.2025.107089.